Measuring Changes in Snowpack SWE Continuously on a Landscape Scale Using Lake Water Pressure

HAMISH D. PRITCHARD,[a,b] DANIEL FARINOTTI,[b,c] AND STEVEN COLWELL[a]

[a] *British Antarctic Survey, Cambridge, United Kingdom*
[b] *Swiss Federal Institute for Forest, Snow and Landscape Research WSL, Birmensdorf, Switzerland*
[c] *Laboratory of Hydraulics, Hydrology and Glaciology (VAW), ETH Zurich, Zurich, Switzerland*

(Manuscript received 24 August 2020, in final form 11 November 2020)

ABSTRACT: The seasonal snowpack is a globally important water resource that is notoriously difficult to measure. Existing instruments make measurements of falling or accumulating snow water equivalent (SWE) that are susceptible to bias, and most represent only a point in the landscape. Furthermore, the global array of SWE sensors is too sparse and too poorly distributed adequately to constrain snow in weather and climate models. We present a new approach to monitoring snowpack SWE from time series of lake water pressure. We tested our method in the lowland Finnish Arctic and in an alpine valley and high-mountain cirque in Switzerland and found that we could measure changes in SWE and their uncertainty through snowfalls with little bias and with an uncertainty comparable to or better than that achievable by other instruments. More importantly, our method inherently senses change over the whole lake surface, an area in this study up to 10.95 km^2, or 274 million times larger than the nearest pluviometer. This large scale makes our measurements directly comparable to the grid cells of weather and climate models. We find, for example, snowfall biases of up to 100% in operational forecast models AROME-Arctic and COSMO-1. Seasonally frozen lakes are widely distributed at high latitudes and are particularly common in mountain ranges, hence our new method is particularly well suited to the widespread, autonomous monitoring of snow-water resources in remote areas that are largely unmonitored today. This is potentially transformative in reducing uncertainty in regional precipitation and runoff in seasonally cold climates.

SIGNIFICANCE STATEMENT: This work demonstrates a new method for measuring the water supplied by snowfall on the landscape scale. We find that we can measure accurately and precisely the changing water content of a snowpack by monitoring water pressure in lakes. Monitoring water pressure is relatively simple, cheap, and robust, and pressure changes represent the whole lake surface, which can be an area of many square kilometers. This makes our measurements comparable in size to the grid cells used by weather models, removing one of the major sources of uncertainty when calibrating these models to conventional point measurements of snow. Our method could therefore lead to an improved understanding of regional precipitation and runoff in seasonally cold climates.

KEYWORDS: Snow cover; Water budget/balance; Instrumentation/sensors; Surface observations; Mountain meteorology

1. Introduction

Snowfall seasonally covers 46 million km^2 of Earth's surface (NSIDC 2020), a third of all land, and dominates the water supply for one-sixth of the world's population and a quarter of global GDP (Barnett et al. 2005). By storing water in winter and releasing it in the warm growing season when it is most valuable, snow is worth up to $88 billion per year in the western United States alone (Sturm et al. 2017). Despite its importance, however, the snow water equivalent (SWE) of both falling and accumulated snow are poorly observed, particularly in mountains. Measurements of falling and accumulated snow are used to develop, test, and drive weather, climate, and hydrology models; hence, the lack of observations constitutes a critical observational gap in the terrestrial water budget (McCrary et al. 2017; Yao et al. 2018; Xu et al. 2019; Yoon et al. 2019). This gap is the most important unsolved problem in snow hydrology (Dozier et al. 2016), and the ultimate cause of large water resource uncertainties and biases, particularly in the headwaters of High Mountain Asia's major river basins (Yatagai et al. 2012; Smith and Bookhagen 2018; Wortmann et al. 2018; Bannister et al. 2019; Lievens et al. 2019; Momblanch et al. 2019; Orsolini et al. 2019; Yoon et al. 2019).

Measuring snow is notoriously difficult and the lack of data reflects a global array of instruments and manual measurements that, despite considerable advances, remains too sparse, biased toward lower altitudes and latitudes, and not sufficiently representative of snow variability in the landscape (e.g., Sturm et al. 2010; Dozier et al. 2016; Lievens et al. 2019). The World Meteorological Organization (WMO) recommends a precipitation sampling density of 0.4 stations per 100 km^2 for mountainous regions but this is rarely achieved (Haberkorn 2019). In relatively well-monitored Europe and Russia, for example,

Denotes content that is immediately available upon publication as open access.

Corresponding author: Hamish Pritchard, hprit@bas.ac.uk

DOI: 10.1175/JHM-D-20-0206.1

Publisher's Note: This article was revised on 16 April 2021 to fix a production error that caused a distortion in the presentation of Fig. 10b.

snowfall or snowpack SWE is observed manually at 4753 sites at intervals from 1 day to 1 year, but at only 121 sites at a frequency comparable to weather-model time steps (i.e., hours), and of these sites, only 38 are above 2000-m altitude (Haberkorn 2019). Although a quarter of Switzerland (~10 000 km^2) is mountainous terrain above 2000 m, the SWE station density is only 0.2 stations per 100 km^2 (www.meteoswiss.admin.ch). Furthermore, these measurements are primarily intended for avalanche warning and so are neither verified nor bias corrected for climatology (Salzmann et al. 2014). In Finland, where snowfall dominates annual runoff throughout the country (Barnett et al. 2005), reportedly no SWE measurements are routinely made at greater than monthly frequency (Haberkorn 2019). Of the ~100 000 weather stations with daily data in the Global Historical Climate Network database (Menne et al. 2012), only one permanent precipitation-monitoring station currently represents the 566 000 km^2 of High Mountain Asia above 4000-m altitude.

There is no standardized method for measuring falling or accumulated SWE, and although numerous field-based approaches have been developed, all have important limitations. These help explain the paucity of existing observations. Existing approaches include automated snow pillows and scales, heated pluviometers, lysimeters, totalizers, gamma radiometers, electrical impedance sensors (Sommer and Fiel 2009), GPS receivers (e.g., Koch et al. 2014), cosmic-ray neutron sensors (e.g., Schattan et al. 2017), and geolysimeters (e.g., Smith et al. 2017b), plus manual snowpits, cores, and radar surveys. The limitations of these approaches include infrequent sampling, limited measurable range, a high cost of labor, instruments, installation or maintenance, high power requirements, dependence on local empirical relationships for calibration, uncertainties in deriving SWE indirectly from proxies, risk of environmental contamination (from snow pillows), and instrumental undercatch or overcatch bias (e.g., UNESCO/IASH/WMO 1970; Koch et al. 2014; Kinar and Pomeroy 2015; Stranden et al. 2015; Grossi et al. 2017; Janowicz et al. 2017; Schattan et al. 2017; Smith et al. 2017a; Smith et al. 2017a; Steiner et al. 2018; Ménard et al. 2019). Commonly used pluviometers suffer, for example, from biases as great as −78% in strong winds (Goodison 1998). Even the more sophisticated but uncommon double-fence intercomparison reference pluviometer has an average bias from −3 to −6%, and up to −50% in strong winds relative to observed snowfall among bushes, which is considered the true snowfall in the natural environment (Yang 2014). Geolysimeters that sense changes in borehole water pressure are able to avoid such wind biases and have been shown experimentally to be sensitive to snow loading on hourly time scales over areas of several square kilometers (Smith et al. 2017b). However, they require boreholes from tens to hundreds of meters deep drilled into specific geological formations that are confined, saturated, and porous (van der Kamp and Maathuis 1991; Smith et al. 2017b; Tipman 2020), and because such boreholes are rare and relatively complex and expensive to survey and drill, this method is not widely used. Neutron and gamma radiometers are commercially available and somewhat more common but their measurement sensitivity saturates at ~0.15 m SWE (Hydroinnova 2020) and ~0.60 m SWE (Campbell 2020), respectively, and their installation costs, along with those for snow pillows and snow scales, are relatively high at USD $21,000, $34,000, $17,000, and $28,000, respectively (including power supply, data transmission, and temperature and snow depth sensors where needed, prices circa 2015) (e.g., Stranden et al. 2015). Perhaps the greatest limitation of the established approaches, however, is their small observed footprints relative to the spatial variability of SWE and to the size of grid cells in weather and snow hydrology models (typically ≥0.5 km) (e.g., Anderton et al. 2004; Fiddes et al. 2019). Their footprint diameters range from 0.16 to 0.23 m (pluviometers in this study) to ~10 m (e.g., gamma radiometers; Campbell 2020), or exceptionally up to ~250 m for neutron sensors (Schattan et al. 2017). Across all of Europe, there are only eight of these larger-footprint stations used operationally (Haberkorn 2019). Given their small footprint size, the vast majority of observations are effectively point measurements, and these represent poorly the heterogeneity of falling and accumulated SWE in mountain landscapes. A detailed assessment of snowpack-SWE variability yielded, for example, standard deviations in point measurements of 21% and 12% in flat terrain over plots as small as 20 m × 8 m and 40 m × 40 m (Haberkorn 2019). Point observations from SNOTEL snow pillows were found not to represent adequately SWE at gridcell scales of 1–16 km^2, with biases up to 200% (Molotch and Bales 2005). Consequently, even in the few locations with existing instruments, and assuming that they produce accurate, unbiased measurements at those locations, the spatial-sampling bias introduced by these point-scale measurements into gridded products and models is likely substantial, and typically unknown (Momblanch et al. 2019).

To improve the accuracy of the terrestrial water budget in seasonally cold regions, more accurate and extensive SWE observations are needed, preferably at the subdaily intervals and large spatial extent of gridded model calculations. A larger observation network expanded farther into mountain ranges could be achieved with autonomous sensors that combine low cost, simplicity, robustness and low power consumption. We present a new approach to measuring SWE in a changing snowpack that shows great promise in meeting these requirements.

2. Hypothesis

We hypothesized that we could use natural lakes in the landscape to measure changing SWE in a way broadly similar to a snow pillow, but on a much larger scale. Snow pillows measure changes in SWE by monitoring fluid pressure in a sealed bladder as the mass of snow resting on the pillow changes. Although lakes are not sealed vessels, we hypothesized that in freezing conditions, changes to snowpack SWE on a lake surface should produce equivalent (though transient) changes in water pressure at the lake bed that would be simple to measure. This develops further the observation that snow can contribute to lake water level in closed basins over seasonal time scales (e.g., van der Kamp et al. 2008), and is an appealing idea for several reasons:

1) Water-pressure gauges are commonly available, relatively low cost, easy to deploy and robust, and they can monitor pressure precisely, continuously, and autonomously.

2) Water pressure responds directly and immediately to mass change. Pressure could therefore be a direct and sensitive measure of changing SWE, rather than an indirect proxy for SWE.
3) Lakes are in hydrostatic equilibrium so the pressure signal measured at any location reflects the average mass added over the whole lake area. Pressure measured at a point could therefore allow SWE to be measured on a large, "landscape" scale.

The main challenge with this approach comes from the more complex nature of pressure signals in a natural lake than those from the sealed system of a snow pillow. SWE signals on a lake would likely be transient because lake drainage can respond to compensate for the pressure change. Furthermore, there are other variable water fluxes that can affect lake water pressure. In thawed conditions, lake levels and water pressure respond in a complicated way to a combination of factors including 1) precipitation, evaporation and catchment runoff into the lake that vary on short (approximately hourly) time scales, and 2) more slowly varying contributions from lake drainage and subsurface lateral flow, as well as from aquifer recharge and return flow in the catchment. Lake-level fluctuations should, however, be simplified in sustained freezing conditions when precipitation in the catchment is stored as snow rather than running off, and when evaporation is reduced because of both low temperatures and the formation of an ice cover. Snow falling directly onto the lake itself should produce an instantaneous water pressure signal, distinct from the more slowly varying winter background pressure trends.

Specifically, when the catchment and the lake surface are frozen, this approach should allow changes in *snowpack* SWE on the lake ice to be observed. The change would reflect the sum of physical changes to the snowpack water content through precipitation, wind reworking and sublimation (e.g., Meyer et al. 2012), thus providing a signal equivalent to that observed by snow pillows, scales, and geolysimeters, or indirectly by gamma, neutron, impedance, or GPS-based automatic SWE instruments. When wind and sublimation effects are small, this would closely approximate accumulated precipitation, i.e., *snowfall* SWE, which is the signal observed by pluviometers and totalizers and a primary output of weather models and input to hydrology models. Provided that the snowpack pressure signal can be separated from background pressure trends, lake-bed pressure sensing thus offers the potential to make rapid, direct and autonomous measurements of changing SWE over areas that are very much larger than the footprints of established field instruments.

3. Experimental setup

We tested this hypothesis at three sites: 1) Orajärvi, a 10.95-km^2 lake in the lowland Finnish Arctic at 180-m altitude; 2) Silsersee, a 4.12-km^2 Swiss alpine valley lake at 1800-m altitude; and 3) Tomasee, a 0.025-km^2, high-alpine cirque lake at 2345-m altitude, and the source of the River Rhine (Fig. 1). In each case, we deployed commercially available, high-precision water-pressure sensors (nominal precision 0.1% full scale) on the lake bed, either in advance of the winter freeze-up or via a hole drilled through the winter ice cover.

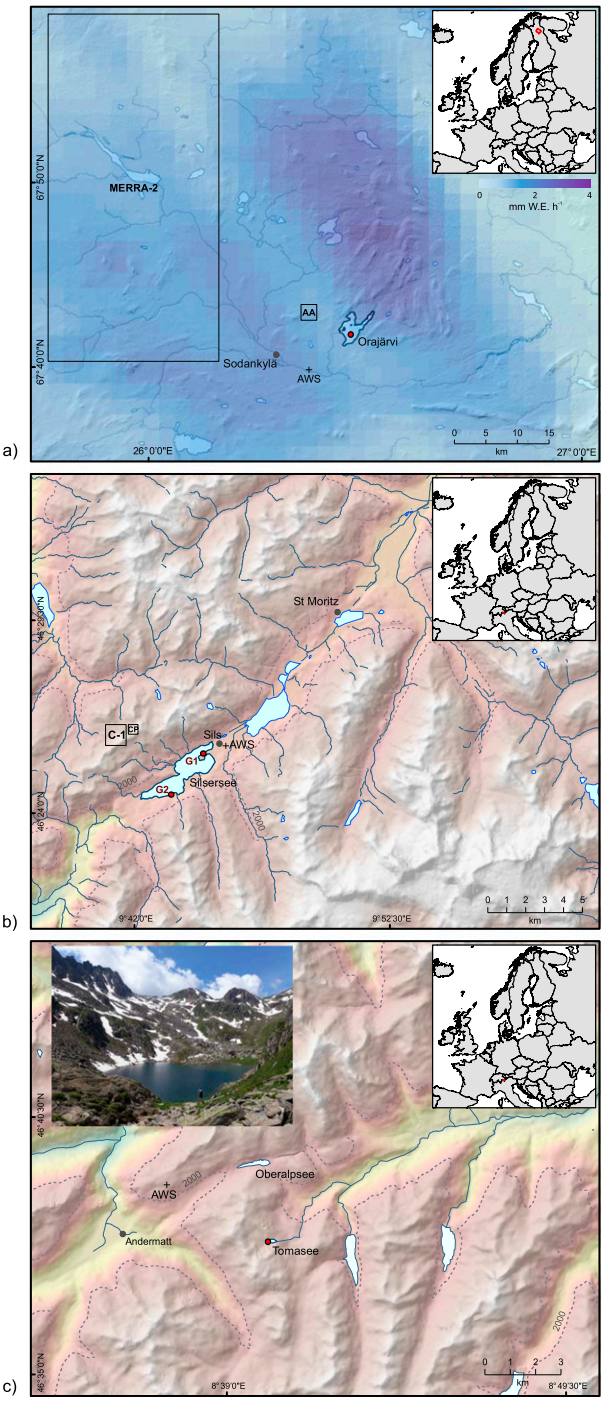

FIG. 1. Locations of lakes (a) Orajärvi, Finland; (b) Silsersee, Switzerland; and (c) Tomasee, Switzerland. Red dots indicate gauge locations, crosses indicate automatic weather stations (AWS). Panel (a) also shows gridded precipitation (blue color scale) for 0400 LT 6 Apr 2018 from the AROME-Arctic forecast model at 2.5-km cell size (size indicated by box AA), and the size of a MERRA-2 grid cell. Panel (b) shows the locations of gauges G1 and G2, and boxes C-1 and CP indicate the 1.1-km and 500-m gridcell sizes of the Cosmo-1 and CombiPrecip precipitation products. Inset photo in (c) shows Tomasee in summer.

To maximize gauge sensitivity, we specified a relatively small pressure range of 1–10 bar and positioned our gauges in water depths of 1–5 m. We deployed the Orajärvi sensor in March–May 2018, at 1 km from shore with a logger box on the ice, and the others with logger boxes on the shore for periods through winters 2018/19 and 2019/20 (Fig. 2). All three lakes froze over completely during the studied periods. The gauges recorded water pressure and water temperature, and were naturally ventilated with breather tubes (open to the air at the logger box) to compensate for atmospheric pressure changes. We also used a thermistor on the ground at each logger-box site to measure snow-base temperatures, allowing us to detect the onset of snowmelt runoff in spring. The Orajärvi pressure gauge logged every minute, the other sites every 10 min. The Tomasee logger was also set up to transmit hourly averaged data over a satellite network. Transmission happened every 4 h. At Silsersee we deployed one gauge in 2018/19 (G1) and a second gauge (G2) running concurrently with G1 from late February to early August 2020 (Fig. 1b). All loggers were powered by 12-V lead-acid batteries. Based on laboratory tests, average consumption with and without satellite transmission was 2.1 and 1.4 Ah month^{-1}, respectively. The deployments required no groundworks and left no trace after removal. The equipment cost of each installation (including pressure gauge, logger, modem, thermistor, battery, and case) was less than USD $3,000.

We compared our results to observations from the nearest permanent automatic weather station (AWS). For Orajärvi, this was the AWS of the Finnish Meteorological Institute at Sodankylä (WIGOS-ID 0-20000-0-02836, 7 km from Orajärvi); for Silsersee, it was the MeteoSwiss AWS at Sils (WIGOS-ID 0-20000-0-06779, adjacent to Silsersee), and for Tomasee, it was the MeteoSwiss AWS at Gütsch Andermatt (WIGOS-ID 0-20000-0-06750, 5 km away) (Fig. 1). Data from these stations are publicly available.

4. Characteristics of the observed water-pressure time series

In winter, the time series of water pressure P from all three lakes showed two dominant signals: (i) a declining pressure trend of several centimeters to decimeters water equivalent (W.E.) over weeks to months, punctuated by (ii) abrupt jumps in pressure from millimeters to centimeters water equivalent on hourly to daily time scales (Fig. 2). The declining trends demonstrate that there was net drainage of water out of the lakes through winter, while the abrupt, shorter-duration pressure jumps indicate net mass gains. Most crucially, the timing and magnitude of these pressure jumps corresponded closely to snow precipitation as independently observed by the nearby AWS (Fig. 1), thus supporting our working hypothesis.

We note one other large pressure increase that coincided with the onset of the spring thaw, that we interpret as being due to snowmelt runoff to the lake (e.g., from 17 April 2019 in Fig. 2d). This interpretation is supported by our thermistor data showing that the lakeshore ground temperatures rose to 0°C and remained constant for several days, which is indicative of a thawing snowpack with liquid water percolating to the base. This period of constant temperature was followed by marked diurnal cycles in both ground and water temperatures, with peaks above 0°C, indicating loss of the snowpack and lake-ice cover (e.g., after 22 April 2019 in Fig. 2c, upper panel).

Modulating slightly the dominant pressure changes described above, we observed second-order signals associated with strong winds. A periodic oscillation with frequency around 25 min and amplitude up to 1 mm was sometimes apparent at Orajärvi, the largest and least sheltered of the three lakes (Fig. 3). This frequency agrees with that expected of a seiche wave with a single node, given the average lake depth (4.4 m) and length (4.8 km) (Kalff 2002), and we interpret the signal as the result of oscillating wind-driven swell. Temporal averaging over hourly periods reduces the amplitude of the oscillations to ~0.2 mm (Fig. 3).

Similar but less clearly wave-like pressure spikes with amplitude ~2 mm and lasting typically ~1 h occurred in the two concurrent pressure time series from Silsersee (from gauges 1 and 2 separated by 3 km, Fig. 1b). A train of spikes occurred, for example, around 27–28 February 2020, one of the windiest periods in our record (Fig. 2c), with the signals being in apparent antiphase between the two gauges (Fig. 4). Similarly, over a 3-week period in 2019, the water pressure recorded at Silsersee spiked by up to +2 mm W.E. during winds gusting to gale force (e.g., gray arrow in Fig. 6c).

We interpret these transient pressure anomalies during strong winds as some combination of the swell effects described above and potentially localized air pressure anomalies in the vicinity of each gauge, on either windward slopes (locally high pressure) or leeward slopes (locally low pressure) on the lake shore. The interpretation of swell is supported by spikes in the water temperature data. Indeed, the temperature spikes coincide with or follow high winds as the water-pressure anomalies begin to appear, suggesting wind-driven disturbance of the temperature-stratified lake water below the ice cover (Fig. 4). Local air pressure anomalies could contribute to temporary water-pressure artifacts because the gauges automatically compensate for air pressure locally via their vent tubes. The antiphasing of the spikes shown in Fig. 4 suggest that the Silsersee lakeshore gauge logger sites were respectively leeward and windward to the wind at this time. Averaging of these two series reduced the amplitude of the transient spikes to ~0.2 mm (Fig. 4).

Although these second-order, antiphase pressure signals are present in the two time series from Silsersee, the series are highly correlated over the full 5-month period of overlap (Fig. 5, gray dots), the particularly windy period shown in Fig. 4, and the less windy period spanning the large snowfall event on 3 March 2020 (Fig. 5, green dots and inset plot, and Fig. 6e). The Pearson correlation coefficients for these three periods are 0.999 98, 0.948 41, and 0.995 09, respectively. The greatest disagreements correspond with the period of strong wind shown in Fig. 4.

5. The SWE method: Quantifying the change in snowpack SWE and its uncertainty from the pressure time series

As described above, the time series of water pressure consisted of two dominant components: a slow pressure drop due

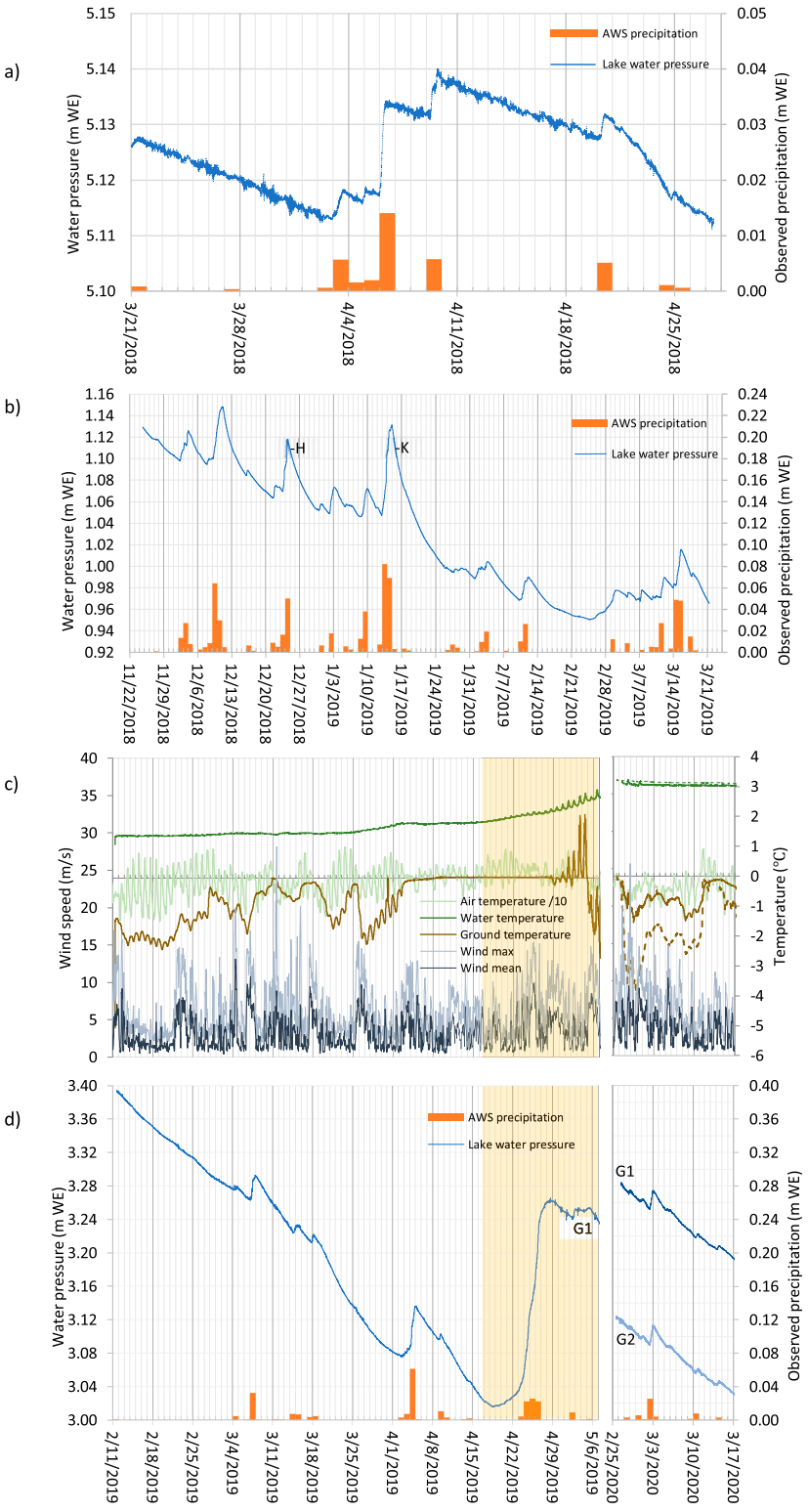

FIG. 2. Lake water pressure time series and precipitation observations from the nearest AWS from lakes (a) Orajärvi, (b) Tomasee, and (d) Silsersee with air, ground, and water temperatures and (c) wind speeds and the period affected by the spring thaw (yellow background). G1 and G2 in (d) refer to the two pressure gauges run concurrently in 2020. Points H and K in (b) are referred to in the text and indicate periods of equal water pressure but differing drainage rates.

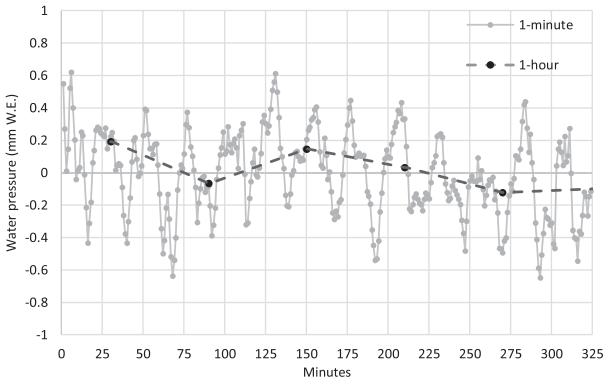

FIG. 3. High-frequency Orajärvi water pressure signals (after detrending; mm W.E.) during dry weather on 4 Apr 2018, showing averages over 1 min and 1 h.

to net lake drainage through winter, and pressure jumps primarily associated with snow accumulation, i.e., changes in snowpack SWE. To quantify the change in snowpack SWE (dP_{SWE}) through a snowfall event from the overall change in water pressure (dP), the component of the pressure signal due to lake drainage (dP_D) must be calculated for the same period and subtracted from dP (e.g., Fig. 6a).

The size of the drainage component over a snowfall is determined by the rate of pressure change due to drainage ($\dot{D} = dP_D/dt$). This "drainage rate" can be calculated directly from the pressure time series during dry weather. Over multiday periods of dry weather (e.g., from 18 to 26 January 2019 in Fig. 2b), the decline in water pressure due to net drainage out of the lake was approximately exponential, in agreement with theory (de Zeeuw 1973), but over shorter (e.g., daily) time scales, this decline can be well approximated by an ordinary least squares linear fit. Linear fits to 50 dry periods each ~1 day long in the Tomasee time series had an average $R^2 = 0.985$, for example (Table 1, Fig. 2b).

The drainage rate $\dot{D}$ as a function of P is not constant. It can, for example, increase in response to snow loading on the lake. For each snowfall event (of typically ~1-day duration, Fig. 2), it is therefore necessary to calculate how the drainage rate evolved through the event. To do this, we calculated the change in drainage rate in response to changing P using the total pressure change ΔP observed over each snowfall and the change in gradient of the two linear fits ($\dot{D}_1$ *and* $\dot{D}_2$) to the pressure time series from the immediate pre- and post-snowfall dry periods that bracket each event,

$$\frac{d\dot{D}}{dP} = \frac{\dot{D}_2 - \dot{D}_1}{\Delta P}.$$

We term these pre- and post-snowfall dry periods used to calculate $\dot{D}_1$ and $\dot{D}_2$ as period 1 and period 2, respectively (e.g., the solid red and solid yellow lines in Fig. 6). In these examples, we manually picked the snowfall start and end points based on the breaks in slope in the pressure time series, and defined

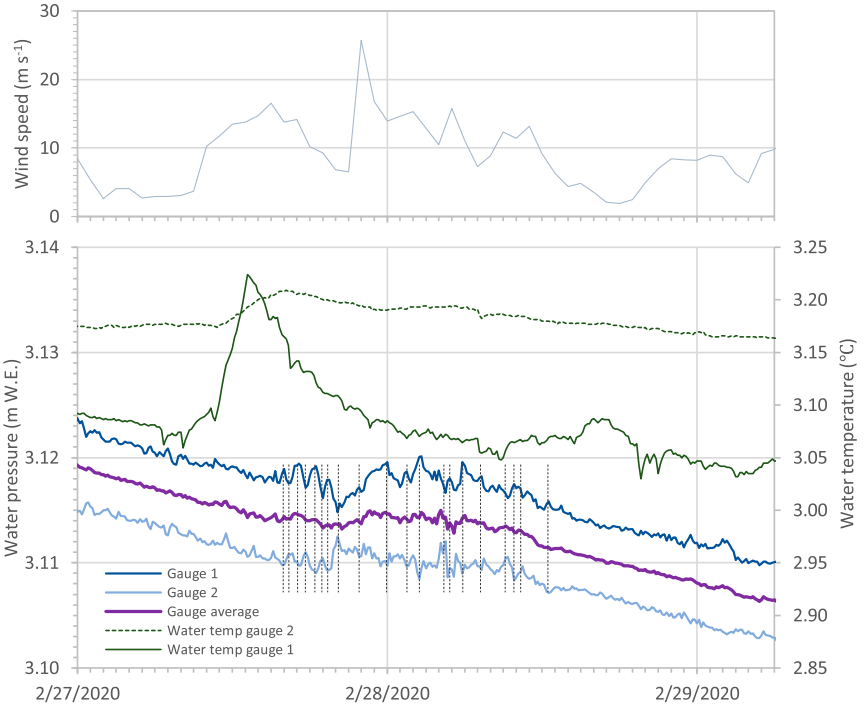

FIG. 4. Silsersee gauge 1 and 2 time series of hourly maximum wind speed (gray line), water pressure (blue lines), and water temperature (green lines) during a period of high winds (Fig. 2b). The average pressure of the two series is given (purple). Vertical dashed lines highlight coincident pressure spikes of opposite sign (antiphase) in the two time series.

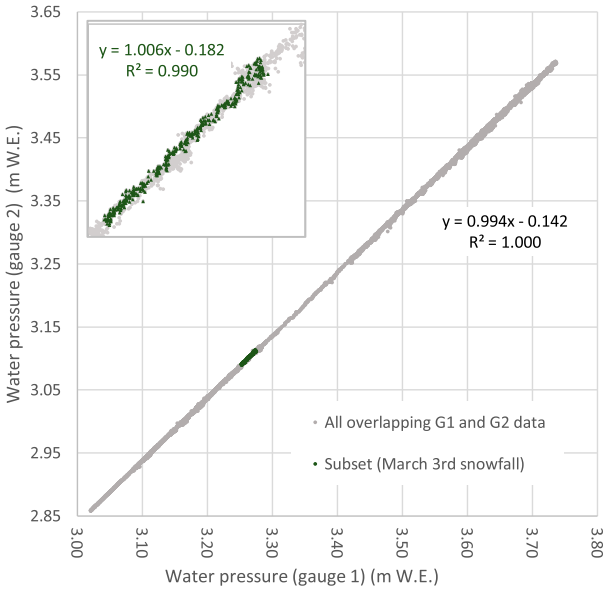

FIG. 5. Water pressure time series for Silsersee gauge 1 vs gauge 2 for the full overlapping period (26 Feb–6 Aug 2020, gray) and a subset (green) spanning the period used to quantify the snowfall on 3 Mar 2020 (Fig. 8d) (from 1940 LT 1 Mar to 1050 LT 4 Mar 2020). Equations and R^2 values are for linear regressions to each set. Note that these sensors were deployed at slightly different water depths and so have different absolute pressures, though the range of the axes is the same.

period 1 and period 2 as spanning approximately 1 day before and after these breakpoints, respectively.

This relationship allowed us to calculate the drainage rate at all times t through each snowfall as

$$\dot{D}(t,P) = \dot{D}_1 + (d\dot{D}/dP)[P(t) - P_{t0}],$$

where P_{t0} is the pressure at the end of period 1 (immediately before the start of the snowfall). From this, we integrated the drainage-related pressure changes to determine the cumulative magnitude of the drainage signal dP_D at time t,

$$dP_D(t) = \int_{t0}^{t} \dot{D}dt.$$

In this way, our calculated drainage progressively transitioned from the period-1 drainage rate to the period-2 rate as a function of varying water pressure during each snowfall. This is most clearly shown in Fig. 6c as the deviation of the solid black, calculated-drainage line from the extrapolated period-1 gradient (dashed red line). By subtracting the calculated drainage component from dP, we were able to calculate total dP_{SWE} over a given time interval as

$$dP_{\mathrm{SWE}} = dP - dP_D.$$

This approach (using the pre- and post-snowfall period 1 and period 2 to calculate dP_D) is suited to calculating dP_{SWE} after an event, and following ~1 day of dry weather. To calculate dP_{SWE} in real time, the drainage component could be estimated using the drainage rate from period 1 and drainage rates observed earlier in the time series at the same pressures, if available, without having to wait to observe the post-snowfall period 2. The implicit assumption of a unique relationship between lake pressure and drainage could introduce some bias, however, because drainage occasionally exhibits hysteresis, with different drainage rates occurring for the same pressure. An example is the contrast in gradients around points H and K in the Tomasee time series in Fig. 2b. Such hysteresis could result from the partial closure of the lake outlet by freezing, or the enlargement of the channel by melting in response to increased water flux (particularly if the channel is small, as at Tomasee where the outlet cross section is on the order of 1 m^2).

With the relatively large hysteresis effect in this example from Tomasee (between points H and K, Fig. 2b), a low bias in real-time estimates of dP_{SWE} of 10% (12 mm W.E.) in the cumulative snowfall total would result from using the gradient around point H (on 25 December 2018) to calculate dP_{SWE} during the later snowfall around 11–12 January 2019, rather than waiting to observe the post-snowfall gradient at point K, on the 15 January 2019. Such bias can be corrected retrospectively, however, once period 2 has been observed. Hereafter, the dP_{SWE} that we report is calculated retrospectively, using both periods 1 and 2.

Uncertainty in dP_{SWE} (denoted $\varepsilon_{\mathrm{SWE}}$) arises from a combination of instrumental uncertainty in the pressure measurements (ε_i), uncertainty in dP_D (denoted ε_d), and the effects of lake swell and wind spikes. These sources of uncertainty can also be quantified from the pressure data. We calculated the relative instrumental uncertainty ε_i from the pressure measured at a constant water depth in a laboratory over an hour (Fig. 7) as ±0.02 mm [two standard errors (2SE)]. As our pressure sensor automatically compensates for nonlinear sensitivity and temperature dependencies, we treat this instrumental uncertainty as fixed.

Drainage uncertainty ϵ_d arises from uncertainty in the linear fits to the data pre- and post-snowfall and the instrumental uncertainty. Using standard error propagation, we calculated ε_d at 2SE for a given time t throughout each snowfall event as

$$\varepsilon_{d(t)} = 2\left\{[\varepsilon_{\dot{D}_1}(1 + t - t_1)]^2 + [\varepsilon_{\dot{D}_2}(1 + t_2 - t)]^2 + \varepsilon_i^2 + \varepsilon_{y_1}^2 + \varepsilon_{y_2}^2\right\}^{1/2},$$

where $\varepsilon_{\dot{D}_1}$ and $\varepsilon_{\dot{D}_2}$ are the SE in gradient for period 1 and period 2, respectively, and εy_1 and εy_1 are the SE of their y estimates (the root of the residual sum of squares divided by the degrees of freedom), t_1 and t_2 are the midpoint times of the linear-fit periods, and ε_i is the instrumental uncertainty. The uncertainties in the y estimates and gradients depend upon both the linearity and spread of the immediate pre- and post-snowfall pressure data. Where present, they therefore include the effects of wind spikes and swell.

We calculated the uncertainty in total dP_{SWE} at the end of an event as

$$\varepsilon_{\mathrm{SWE}} = 2\left(\varepsilon_d^2 + \varepsilon_{y_2}^2 + \varepsilon_i^2\right)^{1/2},$$

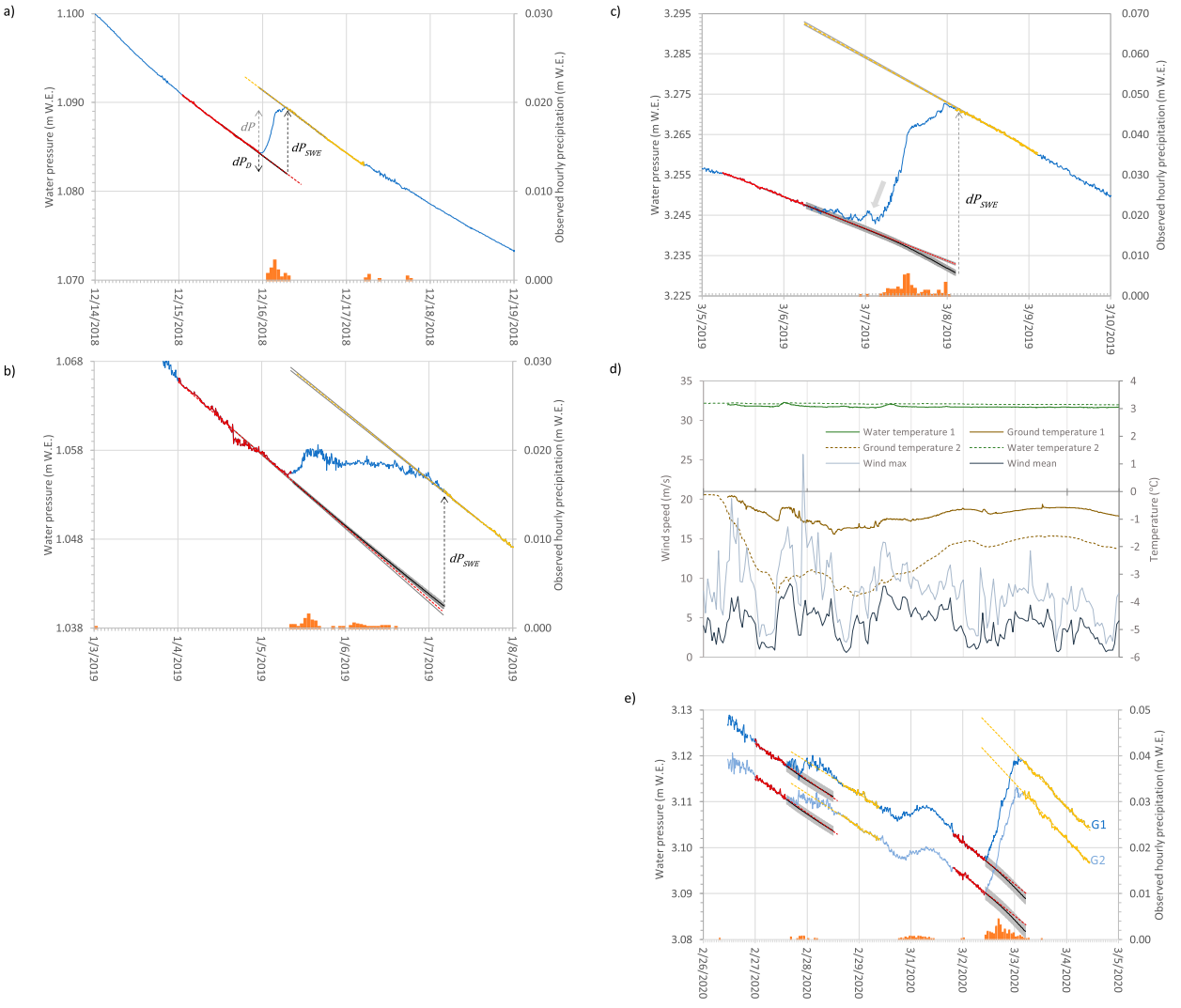

FIG. 6. Water pressure time series (blue lines, left axis) from (a),(b) Tomasee and (c),(e) Silsersee. The dry-weather pressure data before and after each snowfall (period 1 and period 2) are highlighted by solid red and yellow lines, respectively. The gradients of linear fits to these data define the pre- and post-snowfall drainage rates. Dashed red and yellow lines show their linear extrapolation into the intervening snowfall, with diverging gray lines either side [in (a)–(c)] showing their uncertainty. These gradient uncertainties are small and, for simplicity, not shown in (e). The calculated drainage signal (solid black line) as it evolved between these drainage rates is shown, with error bars (solid gray). Labels in (a) show the dP_D and dP_{SWE} components of the observed dP. Also shown is hourly AWS precipitation (orange bars, right axis). Panel (e) shows the concurrent gauge G1 and G2 time series from Silsersee (G1 shifted downward for display) with associated weather and water-temperature records shown above in (d). Uncertainties are two standard errors.

and the uncertainty at intermediate times t during the snowfall (i.e., between period 1 and period 2) as

$$\varepsilon_{\mathrm{SWE}(t)} = 2\left(\varepsilon_{d(t)}^2 + \varepsilon_{P(t)}^2 + \overline{\varepsilon_y}^2 + \varepsilon_i^2\right)^{1/2},$$

where $\varepsilon_{P(t)}$ is the SE of the pressure measurements that are averaged to represent time t (e.g., 60 hourly readings in the Orajärvi data, 6 at the other sites), and $\overline{\varepsilon_y}$ is the mean of εy_1 and εy_2 at 2SE, used here to estimate the uncertainty caused by swell and wind spikes that contribute to the spread around the pre- and post-snowfall linear fits. This estimate is required because we cannot directly quantify the swell and wind effects during a snowfall (such effects can only be distinguished from the linear dry-weather pressure trend, when snowfall, wind, and drainage signals are not present simultaneously).

Other than the wind spikes described, bias in dP_{SWE} potentially arises from the artificial control of water levels in managed reservoirs or natural mass movements such as avalanches into the lakes which do not apply to these results (see section 6), and instrumental drift. The maximum drift for our pressure gauge is specified as 1 mbar yr^{-1}, which equates to 0.028 mm W.E. day^{-1}. Such progressive drift would, however, be captured by period 1 and period 2 and subtracted as if it was

TABLE 1. For a selection of snowfall events, this table shows the components of the pressure time series used to calculate dP_{SWE} and its uncertainty (ε_{SWE}) in column 10, as described in section 5. These include the pre- and post-snowfall pressure gradients and uncertainties ($\dot{D}, \varepsilon_D$), the R^2 and SE in y (ε_y) values for the linear fits, the calculated total pressure change due to drainage (dP_D) and its uncertainty (ε_d), the increase in snowpack SWE (dP_{SWE}) and its uncertainty (ε_{SWE}). Calculated from these, we show the mean dP_{SWE} rate for the example snowfall events in Figs. 2 and 6. The lower six rows show gauge 1, gauge 2, and gauge-mean values (in italics) for the concurrent time series shown in Fig. 6e for snowfalls on 27–28 February and 2–3 March 2020, respectively. Uncertainties are 2SE. Also shown is the total precipitation reported for these periods from the nearest available AWS (Fig. 1) (uncertainties not reported).

Gauge	Snowfall dates	$\dot{D}_1 \pm \varepsilon_{D_1}$ (mm W.E. day^{-1})	R^2	$\dot{D}_2 \pm \varepsilon_{D_2}$ (mm W.E. day^{-1})	R^2	ε_{y_1} (mm W.E.)	ε_{y_2} (mm W.E.)	$dP_D \pm \varepsilon_d$ (mm W.E.)	$dP_{SWE} \pm \varepsilon_{SWE}$ (mm W.E.) (%)	Mean dP_{SWE} rate (mm W.E. h^{-1})	AWS precipitation (mm W.E.)
Orajärvi	6–7 Apr 2018 (Fig. 2a)	−0.66 ± 0.07	0.212	−1.48 ± 0.12	0.297	0.68	1.32	−0.56 ± 1.50	17.26 ± 2.00 (12%)	0.52 ± 0.06	16.1
Orajärvi	2–11 Apr 2018 (Fig. 2a)	−1.17 ± 0.003	0.970	1.02 ± 0.004	0.953	1.36	1.17	0.65 ± 1.80	32.79 ± 2.15 (7%)	0.16 ± 0.01	29.8
Tomasee	16 Dec 2018 (Fig. 6a)	−6.97 ± 0.05	0.998	−7.04 ± 0.05	0.999	0.16	0.14	−0.01 ± 0.24	7.31 ± 0.28 (4%)	1.04 ± 0.04	6.7
Tomasee	5–7 Jan 2019 (Fig. 6b)	−8.27 ± 0.14	0.986	−7.56 ± 0.08	0.997	0.75	0.23	0.66 ± 0.94	13.18 ± 0.96 (7%)	0.29 ± 0.02	8.2
Silsersee gauge 1	6–7 Mar 2019 (Fig. 6c)	−7.96 ± 0.11	0.994	−11.25 ± 0.15	0.994	0.37	0.52	−2.19 ± 0.76	41.05 ± 0.81 (2%)	1.58 ± 0.13	32.5
Silsersee gauge 1	27–28 Feb 2020 (Fig. 6e)	−8.36 ± 0.37	0.955	−7.08 ± 0.24	0.965	0.74	0.71	0.61 ± 1.18	4.06 ± 1.24 (31%)	0.11 ± 0.03	3.0
Silsersee gauge 2	27–28 Feb 2020 (Fig. 6e)	−8.45 ± 0.35	0.960	−7.16 ± 0.19	0.979	0.70	0.55	0.46 ± 1.01	4.42 ± 1.07 (24%)	0.12 ± 0.03	3.0
Silsersee gauge mean	*27–28 Feb 2020*	*−8.41 ± 0.20*	*0.986*	*−7.12 ± 0.08*	*0.996*	*0.42*	*0.23*	*0.51 ± 0.53*	*4.27 ± 0.56 (13%)*	*0.11 ± 0.01*	*3.0*
Silsersee gauge 1	2–3 Mar 2020 (Fig. 6e)	−9.18 ± 0.37	0.966	−11.76 ± 0.15	0.993	0.61	0.74	−1.08 ± 1.25	29.42 ± 1.30 (4%)	1.63 ± 0.07	29.0
Silsersee gauge 2	2–3 Mar 2020 (Fig. 6e)	−8.97 ± 0.42	0.955	−12.16 ± 0.17	0.991	0.68	0.88	−1.39 ± 1.44	29.83 ± 1.50 (5%)	1.66 ± 0.08	29.0
Silsersee gauge mean	*2–3 Mar 2020*	*−9.08 ± 0.19*	*0.990*	*−11.96 ± 0.08*	*0.998*	*0.31*	*0.43*	*−1.27 ± 0.68*	*29.66 ± 0.71 (2%)*	*1.65 ± 0.04*	*29.0*

part of the dP_D signal, and so its impact on dP_{SWE} should be negligible.

From the above, dP_{SWE} bias can be temporarily significant (e.g., up to 2 mm W.E.) during a wind spike but the impact of spikes (and swell) on total ε_{SWE} is limited by their short durations and their high frequencies relative to the length of the fitted periods. It should also be noted that wind spikes introduce only a temporary bias (a pressure jump followed by a drop), and thus they do not propagate through cumulative or total dP_{SWE} calculations. Bias can arise when calculating dP_{SWE} in real time when the post-snowfall drainage rate has not yet been measured (e.g., reaching −10% in the example given), but this can be corrected after the snowfall. Uncertainty is otherwise dominated by imprecision, and is lower for shorter snowfall events and when wind effects are small (e.g., Fig. 6a versus Fig. 6b, showing low-uncertainty and high-uncertainty cases, respectively).

6. Results

a. *Observed changes in snowpack SWE and their uncertainties*

Table 1 and Figs. 8–11 show examples of changes in snowpack SWE and their uncertainties (i.e., dP_{SWE} and ε_{SWE}). When considering the total accumulation of SWE across each snowfall event, we find that Tomasee's 25 snowfalls of winter 2018/19 (Fig. 2b) added an average of 26.64 mm W.E. to the snowpack, with a mean uncertainty (ε_{SWE}) of ±0.75 mm W.E., or ±3% of the total (uncertainty range: from ±0.25 to ±1.62 mm W.E.). During these events, the mean dP_{SWE} rate (the total divided by the duration) for Tomasee was 0.64 ± 0.03 mm W.E. h^{-1} (rate range: 0.12–2.35 mm W.E. h^{-1}, uncertainty range: 0.01–0.07 mm W.E. h^{-1}). The November–March 2018/19 total at Tomasee was 666.1 ± 4.0 mm W.E. When combining the event totals from Silsersee and Orajärvi (Table 1) with those from Tomasee, the ε_{SWE} range was somewhat greater at 0.25–2.15 mm W.E., and 0.01–0.13 mm W.E. h^{-1} for the average rates. We note that ε_{SWE} is independent of dP_{SWE}, i.e., in favorable conditions, uncertainties at the lower end of these ranges were achieved with relatively large snowfalls. The absolute magnitude of the signals that we observed in individual snowfall events ranged from hundreds of tons to hundreds of thousands of tons of water (e.g., from 191 ± 7 t at Tomasee to 359 051 ± 23 543 t at Orajärvi, after Table 1).

As well as the event totals and average rates described above, we resolved individual hourly dP_{SWE} and $\varepsilon_{SWE(t)}$ for the Silsersee snowfall on 6–8 March 2019 (Fig. 10a). To test our uncertainty estimate, we extended these hourly calculations through the dry-weather period 1 and period 2 that bracketed this event, when dP_{SWE} should be near zero as no snow was falling and winds were light ("Linear 1 and 2" symbols in Fig. 10a). These hourly resolved dP_{SWE} values through period 1 and period 2 averaged −0.001 mm W.E. h^{-1} (2SE = 0.04 mm W.E. h^{-1}), while our calculated $\varepsilon_{SWE(t)}$ for these hours averaged 0.92 mm W.E. h^{-1}. From this test, we find that 1) the mean close to zero (−0.001 mm W.E. h^{-1}) indicates negligible bias in our dP_{SWE} calculations, and 2) the

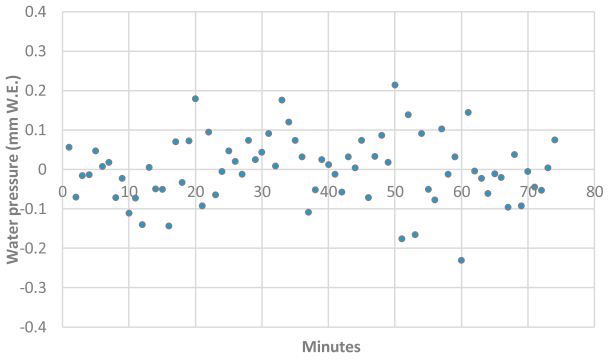

FIG. 7. Instrumental noise (mm W.E.) measured at a constant pressure.

small observed spread (0.04 mm W.E. h^{-1}) indicates that, in light-wind conditions, our ε_{SWE} is a highly conservative estimate of the uncertainty (0.92 mm W.E. h^{-1} in this case (Fig. 10)). The wind spike in this Silsersee example (Fig. 6c), though, temporarily introduced dP_{SWE} artifacts of up to ±1 mm (gray dots in Fig. 10a).

We found that averaging of the pressure time series from two gauges achieved a substantial reduction in uncertainty and bias in dP_{SWE} caused by high wind, particularly when wind artifacts were in antiphase on opposing lakes shores (Fig. 4). For the two Silsersee events in February–March 2020 (Fig. 6e), averaging reduced ε_{SWE} by around 50% relative to the single-gauge uncertainty (Fig. 4 and Table 1, last six rows showing the Silsersee gauge-mean ε_{SWE} (column 10) compared to ε_{SWE} for gauge 1 and gauge 2 individually).

In summary, we were able to quantify uncertainty and bias in dP_{SWE} directly from our pressure time series. We found that uncertainty in total dP_{SWE} for each observed event was approximately ±1 mm W.E., which translates into an uncertainty in average rate over these events of approximately ±0.1 mm W.E. h^{-1}. For individual, hourly resolved dP_{SWE} rates we estimate uncertainty at approximately ±1 mm W.E. h^{-1}, which seems conservative. Our tests indicate that our method is largely unbiased except for occasional pressure spikes during strong winds. These are identifiable and transient, however, and do not propagate into total dP_{SWE}. We also found that we could reduce these biases and other uncertainties substantially (e.g., by ~50%) by averaging two pressure time series from a lake. Because the uncertainty does not scale with total precipitation, the percentage uncertainty varies but averaged ±3% for the 25 Tomasee events, and ranged from ±2% to ±31% in examples chosen to include low- and high-uncertainty events with and without gauge averaging (Table 1).

These uncertainties can be compared to other established methods that, like ours, measure changes in snowpack SWE, and to closely related methods that measure the water content of precipitating snow. In terms of instrumental precision, total daily precipitation measured by pluviometers has an "achievable measurement uncertainty" reported as the largest of ±5% or ±0.1 mm, and for real-time precipitation intensity of rain, ±5 mm h^{-1}, but "significantly worse" than this for the intensity of snowfall as snow tends to stick to the pluviometer walls,

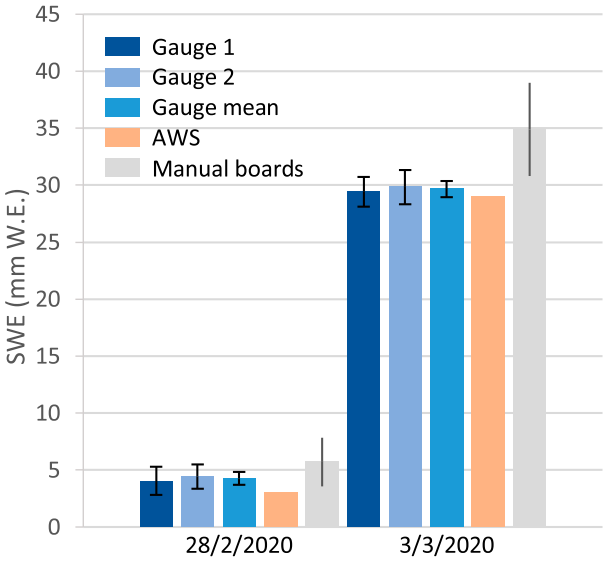

FIG. 8. Silsersee dP_{SWE} measurements from gauge 1 and 2 (Fig. 6e) for snowfalls starting on 28 Feb and 3 Mar 2020 (shades of blue), precipitating snowfall SWE observed at a nearby AWS (orange), and manual observations of accumulated snowpack SWE made using snow boards at nine point locations distributed over the Silsersee lake ice (gray). Board uncertainties are minima (2SE of the point measurements with an assumed measurement uncertainty of 15%). AWS uncertainty is not reported. Note that the board and AWS measurements are not extrapolated to the lake area represented by the gauges.

delaying its measurement (Goodison 1998; WMO 2018). Over various periods, the measurement precision of weighing totalizers is estimated as ±3.8 mm W.E. (Goodison 1998), for snow pillows ±10% (Goodison 1998) or sometimes up to ±29% (Johnson et al. 2015), for gamma radiometry between ±20 mm W.E. (Goodison 1998) and ±90 mm W.E. (Campbell 2020), and for cosmic-ray radiometry, ±13% (Gugerli et al. 2019). The typical precision of our method is therefore similar to or better than these methods, except for pluviometers when measuring a small total daily precipitation < 2 mm (when ±0.1 mm is achievable).

When instrumental biases are also considered, however, the accuracy of these other methods can be considerably poorer than our method. For pluviometers in particular, wind turbulence effects around the gauge can introduce potentially large biases up to −78% (Goodison 1998), or from −15% to −66% (highest at windy sites) for modified, heated tipping-bucket rain gauges, −45% for unheated Hellman pluviometers, and from −2% to +9% for more complex weighing storage gauges with wind shields (Rohrer et al. 2013; Grossi et al. 2017; WMO 2018; Kirkham et al. 2019). The WMO identifies additional pluviometer wetting-loss biases of −1% to −8% for automatic hourly snowfall measurements, or for less frequent (6-hourly) manual observations, biases from −15% to −20% due to wetting and up to −0.8 mm day^{-1} due to evaporation (WMO 2018). Although wind bias strongly dominates the uncertainty of pluviometer measurements of snowfall SWE, globally only 28% of snow pluviometers have wind shielding (Nitu and Wong 2010). For weighing totalizers, bias in total winter SWE

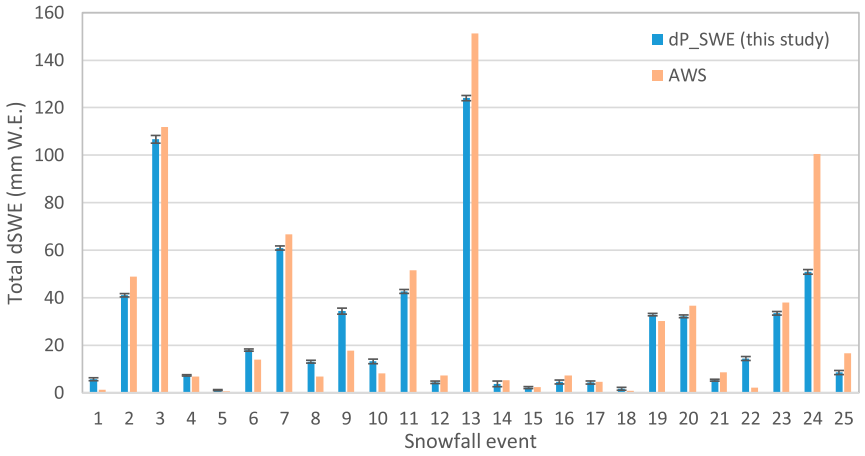

FIG. 9. Tomasee total dP_{SWE} for 25 snowfall events (Fig. 2b) (uncertainties are 2SE) compared to the closest AWS (Fig. 1). AWS uncertainty not reported.

(e.g., due to turbulence) has been observed to reach −20% (Rohrer et al. 2013). Snow pillows are prone to variable low biases due to bridging by ice layers within the snowpack or more commonly high biases of 40%–200% due to the impact of the pillow on snow melting (Johnson and Marks 2004). Cosmic-ray radiometry is less studied but bias of +2% has been reported (Gugerli et al. 2019).

Unlike a pluviometer, totalizer, snow pillow, radiometer, or other sensor on the ground, the water pressure gauge that we use does not interfere with local or, more importantly, lake-scale precipitation, wind, drifting, or other snowpack processes, and so does not introduce these instrumental biases. As we describe above, our hourly resolved dP_{SWE} calculations can be temporarily biased by wind effects, but our event-total measurements are largely unbiased in terms of how accurately they represent the average dP_{SWE} over each lake. This avoidance of instrumental bias is an important advantage of our method.

Our spatially extensive results can be broadly compared to those of the geolysimeter approach, which in certain settings can detect precipitating snowfall (or more specifically, dP_{SWE}) at approximately millimeter precision and hourly time scales without interfering with snow accumulation. Geolysimeter-derived and pluviometer-derived snowfalls correlated highly ($R^2 = 0.94$) at one site over a 6-yr period, with an average bias of 23 mm that may have been due to pluviometer undercatch (Smith et al. 2017b). While a full uncertainty budget is not available for these measurements, we note that the geolysimeter is not prone to the swell effects that we see and would likely be less sensitive to uncertainty in background (e.g., drainage or equivalent) trends. It would be prone to similar localized wind-pressure biases, plus additional uncertainty or bias in the calculation of loading efficiency and Earth tides (Smith et al. 2017b). It may also be limited to lower instrumental precision and accuracy due to the need to accommodate higher water pressures at depth (Tipman 2020). We note also that the response area observed by a geolysimeter is not clearly demarked but loosely defined as having a radius of approximately 10 times the instrument depth, with a decaying sensitivity to loading with distance from the borehole, which may complicate comparisons to pluviometers, gridded precipitation or to independent field observations of changing SWE.

b. *Changes in snowpack SWE compared to manual observations and precipitation from AWS, remote sensing, and weather models*

We compared total snowpack dP_{SWE} derived from our two Silsersee gauges to AWS observations of precipitation by the lake shore, and to manual new-snow SWE measurements that we made on 0.5 m × 0.5 m wooden boards at nine sites distributed over Silsersee (Fig. 8). The dP_{SWE} results from our two independent gauges differed from each other only slightly, by 0.37 and 0.41 mm W.E., respectively, for the two snowfall events shown in Fig. 8, which is small compared to our calculated uncertainties (±1.28 mm W.E. on average for these events) and further suggests that ε_{SWE} is conservative. The equivalent ε_{SWE} calculated from the two pressure series averaged together is ±0.64 mm W.E.

The AWS precipitation and manual SWE results are similar to our gauge results (Fig. 8), though we note the significant limitations of these conventional, point-scale methods in representing precipitation or snowpack accumulation beyond their immediate surroundings: at 4.15 km^2, the Silsersee surface observed by our gauges is over 1.8 million times larger than the combined area of the snow boards, and 206 million times larger than the pluviometer aperture. Furthermore, the uncertainty of the pluviometer measurement is not reported, and may include substantial bias due to undercatch. The uncertainties in the manual board observations shown in Fig. 8 are minima as they represent only the variability between the nine point locations and an estimate of measurement error at those points. The uncertainty involved in scaling these measurements up to the lake area is unknown.

As at Silsersee, the 25 Tomasee events show broad agreement in timing and magnitude with pluviometer data from the closest AWS at Gütsch Andermatt (Fig. 9). Our November–March total at Tomasee (666.1 ± 4.0 mm W.E.) is 11% lower than the 745.4 mm W.E. at the Gütsch Andermatt

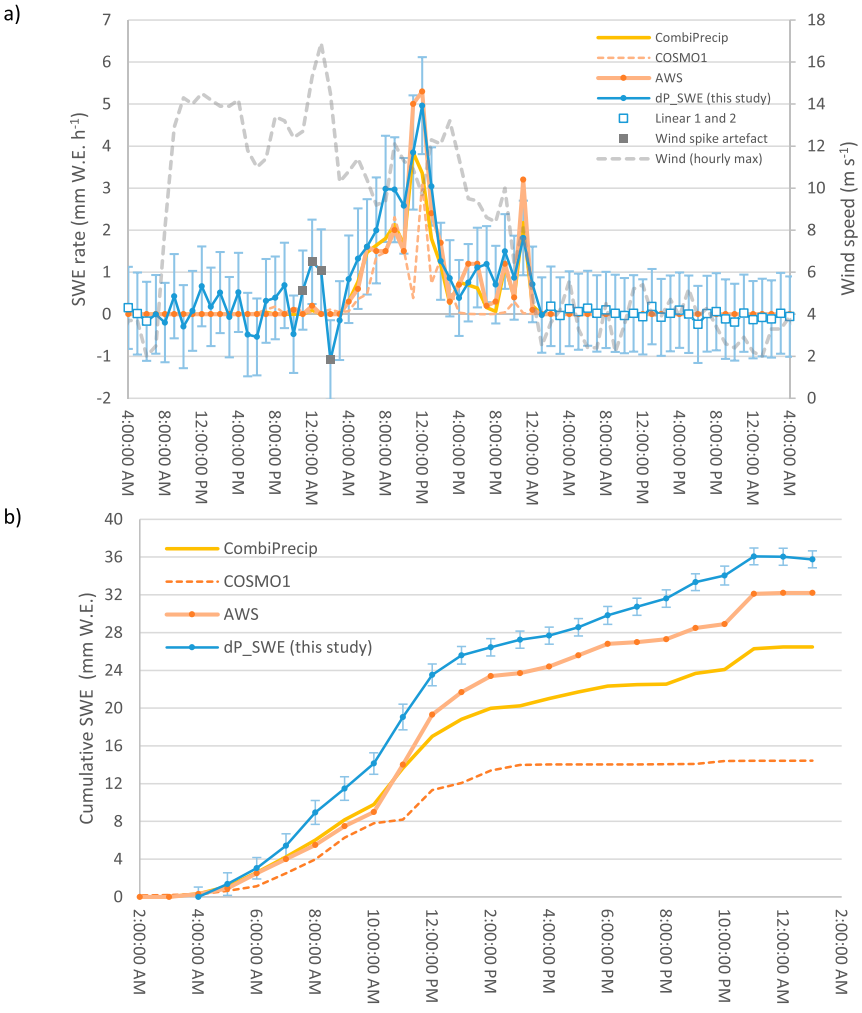

FIG. 10. (a) Hourly dP_{SWE} rates (Silsersee gauge 1) for the 48 h from 0400 LT 6 Mar 2019 (Fig. 6c) together with AWS precipitation and wind speed, and precipitation from gridded products COSMO1 and CombiPrecip for grid cells overlapping Silsersee. No uncertainties are provided for the AWS data and the gridded products. (b) Cumulative SWE estimates from the above.

AWS (no uncertainty reported), though we would again not expect exact agreement given the differences in setting and measurement area (the AWS is 5 km distant from Tomasee and 150 m lower, on a valley side rather than in a cirque, and with a pluviometer area 1.25 million times smaller).

The large spatial extent of our dP_{SWE} measurements make them particularly well suited to testing gridded precipitation products from forecast models and remotely sensed data, which have grid cells on a similar scale. To demonstrate this potential, we compared our hourly dP_{SWE} rates for the 7 March 2019 event on Silsersee (Fig. 2d) to (i) AWS precipitation data, (ii) the statistically combined, 500-m gridded gauge and radar precipitation product CombiPrecip (Sideris et al. 2014) that has 14 cells overlapping the lake, and (iii) the 1.1-km gridded high-resolution Alpine numerical forecast model COSMO-1 (http://www.cosmo-model.org/), with 6 cells overlapping the lake (Fig. 1).

We found close agreement in timing and moderate agreement in rate of dP_{SWE} with precipitation in each of these comparisons (Fig. 10a). Cumulatively over this event, the AWS precipitation total was 5 mm W.E. (13%) lower than our observations (Fig. 10b) which may represent gauge undercatch or a real difference in average precipitation between the small gauge area and the much larger lake. The CombiPrecip observational product (which also uses gauge data) was lower by 29% and the COSMO-1 forecast model by 62%.

It is possible that windblown snow was transported from the surrounding mountains to the valley floor in addition to the newly precipitating frontal snowfall, and that this was measured by the three observational methods but not modeled by COSMO-1. This could explain the lower model total. However, the close agreement in timing of dP_{SWE} rate for all methods and the difference in timing between the peak winds and peak precipitation (Fig. 10a) indicate that wind did not

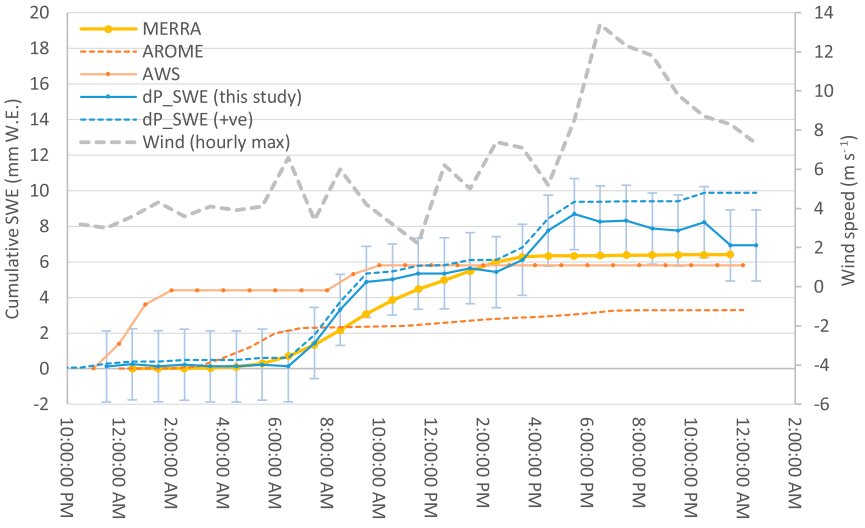

FIG. 11. Cumulative SWE (labeled dP_SWE) and the equivalent cumulative sum using only positive changes to exclude potential erosion signals (labeled dP_SWE (+ve)) on 8–10 Apr 2018 together with AWS precipitation and wind speed, and precipitation from gridded products MERRA-2 and AROME-Arctic for grid cells overlapping Orajärvi. No uncertainties are provided for the AWS data and the gridded products. Note that the snowfall event arrived ~8 h earlier at the AWS, which is 7 km from the lake.

dominate the observed dP_{SWE} rates. More fundamentally, these comparisons show that for whatever reasons, both the conventional observations and the operational model output underestimated the amount of water accumulated by the snowpack on this valley floor, which we observed (Fig. 10b).

We also compared our cumulative dP_{SWE} total for the 6 April 2018 at Orajärvi (Fig. 2b) to (i) precipitation at the nearest AWS, which is the Finnish Meteorological Institute's heated double-fenced intercomparison reference pluviometer located in a small forest clearing 7 km west of the lake, to (ii) MET Norway's AROME-Arctic 2.5-km gridded numerical weather forecast model (with 7 cells partially overlapping the lake), and to (iii) the MERRA-2 (Modern-Era Retrospective Analysis for Research and Applications) global data assimilating 0.625° × 0.5° (~55 km × 27 km) gridded precipitation reanalysis (Fig. 1a). For this event, the timing of snowfall arrival was also in close agreement, but the AWS, AROME-Arctic, and MERRA-2 reported a total accumulation that was 10%, 17%, and 18% lower than our total, respectively. The lower AWS value could again be due to undercatch or a real difference between the two very different sites (the lake is 274 million times larger). We found similarly lower AROME-Arctic and MERRA-2 estimates for smaller snowfalls on 3 and 9 April, but higher estimates for those on 5 and 20 April 2018 (Fig. 2a). These comparisons indicate that substantial snowfall bias is present in these operational precipitation products.

c. *Nonprecipitation changes in snowpack SWE*

Precipitation is the dominant control on our snowpack dP_{SWE} observations (e.g., Fig. 2). However, our method is potentially sensitive to other causes of snowpack mass change, including the net wind transport of snow onto or off the lake and sublimation. We exclude thaw periods when meltwater, condensation and evaporation could also contribute. Exceptions to this exclusion are the spring-onset runoff signal highlighted in Fig. 2d and one less-marked thaw period from 21 to 24 April 2018 in Fig. 2a, when above-freezing daytime air temperatures and an accelerated decline in water pressure suggest evaporation loss from a wet snowpack surface. Snowpack sublimation losses of up to ~1 mm W.E. day^{-1} have been observed elsewhere, at high altitude during high winds and low relative humidity (Stigter et al. 2018), though during snowfall events—when humidity is close to saturation—sublimation losses are typically negligible (e.g., Groot Zwaaftink et al. 2011).

Snowpack erosion and deposition by wind is potentially greater and can occur above a wind speed threshold of 4–11 m s^{-1} for dry, lying snow (Li and Pomeroy 1997)—speeds that were sometimes exceeded during this study. Wind transport would only produce a water pressure signal (dP) if this resulted in a net mass gain or loss from the lake surface, however, i.e., if snow was preferentially eroded from or accumulated by the lake relative to the surrounding terrain. We saw evidence of this only once, at Orajärvi, which is most likely to experience net wind erosion since it sits in a low-relief landscape, has the largest fetch of our lakes, and is surrounded by forest that provides more shelter than the snow-covered lake surface. We observed a water pressure drop after 1800 LT 9 April 2018 (Fig. 11), when winds strengthened to a peak gust speed of 13 m s^{-1} within hours of a fresh snowfall of ~9 mm W.E. in lighter winds. Comparing cumulative dP_{SWE} to the equivalent cumulative sum of only positive changes [shown as dP_SWE (+ve) in Fig. 11, which excludes negative changes that we assume resulted from erosion] provided an erosion estimate of ~2 mm W.E. over 7 h, but this apparent loss was not

significant at the 2SE level. The lack of more obvious wind erosion or deposition signals suggests that, while wind transport of snow may be common, the *net* wind transport of mass onto or off the considered lakes was uncommon, and at most a second-order signal in our observations.

d. The importance of measurement scale

To estimate the magnitude of the scaling uncertainty that arises from limited point sampling of the spatially variable snowpack, we manually measured SWE accumulated since the start of winter at points distributed over Tomasee, the smallest of our lakes. The measurements took place on 25 November 2018. Using a cylindrical snow corer, scales, and a depth probe, we measured snow density at 17 sites and snow depth at 101 sites. Snow depths on top of the lake's distinct, early winter black-ice surface ranged from 4 to 90 cm. The SWE mean was 45.4 mm W.E., the relative standard deviation was 70%, and the 2SE uncertainty in the mean resulting from the spatial variability of the snowpack alone was ±6.4 mm W.E. Even assuming zero measurement error in depth and density, this uncertainty is 8.5 times larger than the mean uncertainty (±0.75 mm W.E.) from our method over 25 Tomasee snowfalls that winter.

Achieving a level of uncertainty comparable to $\varepsilon_{\mathrm{SWE}}$ from such hypothetically error-free manual SWE measurements at Tomasee would require a sample size of around 7000 points, and to achieve the same temporal resolution and scope, these would need to be repeated every hour continuously for several months through the winter. The equivalent calculation based on the board measurements at Silsersee (Fig. 8) (relative standard deviation 12%) implies that around 220 such error-free samples are required. These could be automated by use of 220 snow pillows, for example, at a cost of USD $3.75 million, but this assumes that bridging by ice layers within the snowpack would not introduce measurement bias at some stage. Little improvement in precipitation uncertainty could be achieved by scaling up the number of AWS pluviometers in this way. This is because their inherent biases (section 6a) do not reduce with sample size.

7. Lessons learnt in site selection, instrument deployment, and analysis

In addition to the three sites reported above, we had two unsuccessful deployments of our instruments in Swiss alpine lakes above 2000-m altitude in early February 2019. We failed to drill through a several-meters-thick winter snow and ice pack at Wildsee, while at Oberalpsee (Fig. 1c), the pressure time series was disrupted throughout late winter by unexpectedly frequent (daily) artificial pressure drops as water was released for hydropower. To avoid these problems, we suggest deploying during summer when possible, and in unmanaged lakes or reservoirs where water release is infrequent.

There are few other restrictions on lake selection. While large, kilometer-scale lakes provide better targets for model testing, they tend to be more subject to wind effects. We therefore recommend deploying more than one sensor in each lake to permit averaging, placed at widely spaced locations and with differing aspects along the shore. Lakes must also be large and deep enough to prevent full-depth freezing in winter. Otherwise, the minimum lake diameter for our method is likely to be as small as tens of meters. This is because the flexural strength of a typical ice layer means that it can sustain only a short unsupported span (e.g., up to meters) before failing (Pounder 1965), thus meaning that bridging effects from ice across an inlet or from the shore to the water are not of particular concern. In particular, the fraction of any mass added to the surface of a frozen lake that could be supported by the shore (rather than the water) is small. More localized bridging over inlets along lake shores and river banks may be common (Beltaos and Prowse 2009) but has negligible effect on our method even if the sensor is located in water beneath such a bridge. This is because the accumulating snow mass on the rest of the lake raises the water level everywhere—including in bridged inlets. The size range of suitable lakes is therefore large and this method could, for example, also be applied to small lakes in forest settings where snow accumulation is strongly affected by local vegetation.

Because our observations are insensitive to localized bridging, there is in principle no minimum distance that needs to be maintained between the sensor and the shore. Indeed, we deployed our Silsersee sensors in summer, simply by throwing them in. We paid out several meters of slack cable into the water to limit sensor drag should the ice move, but in practice experienced no problems with ice-rafting or ice-push events: in spring the ice along the shore thawed first, releasing the cables undamaged. We used no anchors or protection for our sensors, though we did secure our logger boxes to trees. In settings where rafting and ice push occur, it would be advisable to deploy the sensors in small, sheltered embayments, or to attach them to dock pilings, for example. Settlement of our sensor into soft sediment (at Orajärvi) lasted no longer than a few hours and was comparable to the period of sensor equilibration to temperature. Any prolonged settlement trend would be removed in the trend-fitting part of the analysis described above.

The minimum sensor depth should be sufficient to allow for the potential water-level lowering over winter, and should also be at least sufficient to avoid the sensor becoming encased in ice as the lake surface freezes downward. Ice encasement would isolate the sensor from the water, and could potentially damage it. It is probably desirable to deploy the sensor below the maximum potential draft of the combined snowpack and snow–ice/slush–ice that forms as the early winter black ice is submerged (Adams and Roulet 1980). This may not be critical, though, as a thick, insulating snow/ice layer that produces a deep draft would tend to hinder growth of new basal ice around the sensor. We further note that as with bridging, any localized grounding of the snow/ice cover during winter does not affect the ability of our method to observe lake-wide dP_{SWE}. The maximum sensor depth is determined by the sensor's specified upper pressure limit minus the expected maximum SWE in an event. The limit for our sensors was ~10 m W.E., hence our deepest deployment of ~5 m at Orajärvi, for example, allowed for a potential 5 m W.E. in any one snowfall event.

Our method should quantify rain-on-snow events as dP_{SWE} signals provided that they do not cause runoff from the catchment, and similarly it should be largely insensitive to short periods of surface thawing without runoff. Other abrupt

signals that may confuse the analysis include avalanches reaching the lake, and upstream dam releases. We detected and quantified two avalanches into Oberalpsee from transmitted data, which were subsequently confirmed by local observers. In hourly averaged pressure data these could be confused with snowfall events, except that they also caused near-instantaneous water-temperature anomalies that snowfalls did not (presumably due to mixing of temperature-stratified water). Our lakes had no upstream dams, and it may be sensible to avoid instrumenting such lakes. Apart from basic information on the size and approximate depth of lakes and the location of dams, no other hydrological or weather data are needed for site selection. Nearby observations of wind speed and air temperature may aid interpretation of the pressure signals, but these are not strictly necessary for quantifying SWE or its uncertainty using our method.

While our method requires a frozen catchment, it is not a requirement that the lake surface is completely or even partially frozen in order to quantify precipitating snowfall. When a snowpack is present, wind speeds below the blowing-snow threshold are preferable for isolating the precipitating snowfall signal, but there is no wind speed limit for measuring the change in *snowpack* SWE. We have not specifically determined the minimum dry-period duration for defining the background drainage rate either side of a snowfall, which is a function of the sample size needed to characterize the trend. However, our ~1-day periods appear long enough to characterize the trends with a simple linear fit. Over longer periods, the more complex, variable exponential nature of the pressure decay is more prominent.

In this study we did not attempt to extrapolate our SWE observations to the catchment scale, but we highlight the value of our measurements as a control for high-resolution weather models. The latter consider the relationship between precipitation and topography on catchment scales, and are the driver of catchment hydrology models. We note, however, that the enhanced drainage of our lakes in response to snow loading, reported here and elsewhere (Gibson and Prowse 2002), naturally implies that lakes in frozen (but not closed) catchments discharge a volume of water equivalent to all of the precipitation that the lakes receive as snow. Typically over a winter season, the lakes experience no net gain of water due to snow falling on them, so this is not added to the catchment snow-water resource. Provided that the lake outlet remains open, snowfall onto lakes directly drives stream discharge, periodically releasing liquid water downstream after each snowfall event, even in catchments that have been deeply frozen for several months.

8. Conclusions

We hypothesized that changes in water pressure in lakes on hourly to daily time scales could provide a direct measure of the water content of accumulating snow averaged over the lake's surface, provided that conditions were cold enough to prevent surface runoff that would complicate this signal. We tested this hypothesis on lakes in the lowland Finnish Arctic as well as in both an alpine valley and high-mountain cirque in Switzerland, and found distinct signals of snowfall in each water-pressure record.

We have shown that after removal of a background lake-drainage signal, these pressure records reveal the change in water content of the snowpack (dP_{SWE}) through snowfall events and also, importantly, its uncertainty (ε_{SWE}). Our method avoids the large but poorly known measurement biases of instruments such as pluviometers and snow pillows because our sensors do not modify the snowfall or snowpack that they observe. Unlike gamma radiometers, impedance and neutron sensors or GPS receivers, our method measures SWE directly rather than a proxy, and it does not lose accuracy or saturate as SWE increases within any reasonable range. Our dP_{SWE} totals are largely unbiased and our measurements achieve an uncertainty comparable to or better than that achievable by other instruments.

An even greater strength of our method is that it inherently averages these dP_{SWE} measurements over the whole lake surface. The lakes in this study were 1.25 million, 206 million, and 274 million times larger than the aperture of the nearest AWS pluviometer. This makes our measurements of a similar scale, and thus directly comparable to, the grid cells of weather models and climate products. The scale of our measurements means that we avoid the potentially large but otherwise unknown scaling biases between the point measurements of conventional instruments and the grid scale of, for example, the CombiPrecip product and COSMO-1 and AROME-Arctic models. We estimate that hundreds to thousands of unbiased point measurements would be required to achieve an accuracy comparable to one of our large-area measurements.

The scale of our observations is a crucial advantage because weather and climate models rely upon calibration and validation by field data for their accuracy. The biases introduced by conventional instruments and, in particular, in scaling up from the point to grid scale, therefore translate into bias in the models relied upon to assess and predict the future of national, regional and global water resources. The few comparisons presented here suggest that even in relatively well-constrained settings, advanced models currently in operational use can be biased by up to ~100%.

In addition to the advantages of accuracy and scale, our instruments are autonomous and their setup and operation is notably simple. Furthermore, because the pressure sensor sits unmoving in still water, it is protected from weather extremes, ultraviolet light and other causes of wear. This makes our instruments among the cheapest to buy, cheapest and easiest to install, most robust, least power-hungry, and least environmentally invasive of any existing instrument.

The obvious limitation of our method is that it is restricted to sites with ponds or lakes in seasonally frozen catchments. There are, however, a large number of potentially suitable water bodies in a wide range of settings where snow observations are currently sparse or absent. For example, Canada has 1 022 000 km^2 of permanent terrestrial water bodies, Russia 465 000 km^2, the United States 309 000 km^2, China 116 000 km^2, Kazakhstan 50 000 km^2, Sweden 35 000 km^2, Finland 30 000 km^2, Greenland 20 000 km^2, Norway 16 600 km^2, Kyrgyzstan 7000 km^2, Iceland 2000 km^2, Switzerland 1700 km^2, and Tajikistan 1500 km^2 (Pekel et al. 2016). Most mountain ranges in particular

are poorly instrumented but rich in widely distributed lakes that provide enormous potential for the application of our method.

Lakes are universally flat, featureless, and restricted to local depressions in the landscape, and so do not represent the natural range of slopes and land-cover types. As demonstrated here, though, they provide large and well-constrained calibration and validation targets for models that explicitly do account for these landscape features.

In summary, the advantages of our new method make it uniquely suited to the widespread monitoring of snow-water resources in remote areas that are largely unmonitored today, and this is potentially transformative in reducing uncertainty in regional precipitation and runoff in seasonally cold climates.

Acknowledgments. This work was funded by the British Antarctic Survey (Natural Environment Research Council) and the Swiss Federal Institute for Forest, Snow and Landscape (WSL). We would particularly like to acknowledge the considerable support of the late Koni Steffen. We are also very grateful for the help of Timo Ryyppö, Laura Rontu, and Bin Cheng of the Finnish Meteorological Institute; Teresa Maaria Valkonen of the Norwegian Meteorological Institute; Christian Allemann of MeteoSchweiz; and Eef van Dongen of ETH Zurich.

Data availability statement. The datasets produced by this study are available from the U.K. Polar Data Centre, British Antarctic Survey at https://doi.org/10.5285/170FC6FA-9878-43FC-9ABD-E6196BAD60A2.

REFERENCES

Adams, W. P., and N. T. Roulet, 1980: Illustration of the roles of snow in the evolution of the winter cover of a lake. *Arctic*, **33**, 17, https://doi.org/10.14430/arctic2550.

Anderton, S. P., S. M. White, and B. Alvera, 2004: Evaluation of spatial variability in snow water equivalent for a high mountain catchment. *Hydrol. Processes*, **18**, 435–453, https://doi.org/10.1002/hyp.1319.

Bannister, D., and Coauthors, 2019: Bias correction of high-resolution regional climate model precipitation output gives the best estimates of precipitation in Himalayan catchments. *J. Geophys. Res. Atmos.*, **124**, 14 220–14 239, https://doi.org/10.1029/2019JD030804.

Barnett, T. P., J. C. Adam, and D. P. Lettenmaier, 2005: Potential impacts of a warming climate on water availability in snow-dominated regions. *Nature*, **438**, 303–309, https://doi.org/10.1038/nature04141.

Beltaos, S., and T. Prowse, 2009: River-ice hydrology in a shrinking cryosphere. *Hydrol. Processes*, **23**, 122–144, https://doi.org/10.1002/hyp.7165.

Campbell, 2020: CS725 Snow Water Equivalent Sensor. Retrieved August 2020, https://www.campbellsci.com/cs725.

de Zeeuw, J. W., 1973: Hydrograph analysis for areas with mainly groundwater runoff. *Theories of Field Drainage and Watershed Runoff*, Vol. II, *Drainage Principle and Applications*, International Institute for Land Reclamation and Improvement, 321–358.

Dozier, J., E. H. Bair, and R. E. Davis, 2016: Estimating the spatial distribution of snow water equivalent in the world's mountains. *WIREs. Water*, **3**, 461–474, https://doi.org/10.1002/wat2.1140.

Fiddes, J., K. Aalstad, and S. Westermann, 2019: Hyper-resolution ensemble-based snow reanalysis in mountain regions using clustering. *Hydrol. Earth Syst. Sci.*, **23**, 4717–4736, https://doi.org/10.5194/hess-23-4717-2019.

Goodison, B. E., P. Y. T. Louie, and D. Yang, 1998: Solid precipitation measurement intercomparison: Final report. Instruments and Observing Methods Rep. 67, WMO/TD-872, 212 pp., https://www.wmo.int/pages/prog/www/IMOP/publications/IOM-67-solid-precip/WMOtd872.pdf.

Gibson, J. J., and T. D. Prowse, 2002: Stable isotopes in river ice: Identifying primary over-winter streamflow signals and their hydrological significance. *Hydrol. Processes*, **16**, 873–890, https://doi.org/10.1002/hyp.366.

Groot Zwaaftink, C. D., H. Löwe, R. Mott, M. Bavay, and M. Lehning, 2011: Drifting snow sublimation: A high-resolution 3-D model with temperature and moisture feedbacks. *J. Geophys. Res.*, **116**, D16107, https://doi.org/10.1029/2011JD015754.

Grossi, G., A. Lendvai, G. Peretti, and R. Ranzi, 2017: Snow precipitation measured by gauges: Systematic error estimation and data series correction in the central Italian Alps. *Water*, **9**, 461, https://doi.org/10.3390/w9070461.

Gugerli, R., N. Salzmann, M. Huss, and D. Desilets, 2019: Continuous and autonomous snow water equivalent measurements by a cosmic ray sensor on an alpine glacier. *Cryosphere*, **13**, 3413–3434, https://doi.org/10.5194/tc-13-3413-2019.

Haberkorn, A., 2019: European Snow Booklet – An Inventory of Snow Measurements in Europe. EnviDat, https://doi.org/10.16904/envidat.59.

Hydroinnova, 2020: SnowFox. Accessed August 2020, http://hydroinnova.com/snow_water.html.

Janowicz, J. R., S. L. Stuefer, K. Sand, and L. Leppänen, 2017: Measuring winter precipitation and snow on the ground in northern polar regions. *Hydrol. Res.*, **48**, 884–901, https://doi.org/10.2166/nh.2017.059.

Johnson, J. B., and D. Marks, 2004: The detection and correction of snow water equivalent pressure sensor errors. *Hydrol. Processes*, **18**, 3513–3525, https://doi.org/10.1002/hyp.5795.

——, A. B. Gelvin, P. Duvoy, G. L. Schaefer, G. Poole, and G. D. Horton, 2015: Performance characteristics of a new electronic snow water equivalent sensor in different climates. *Hydrol. Processes*, **29**, 1418–1433, https://doi.org/10.1002/hyp.10211.

Kalff, J., 2002: *Limnology: Inland Water Ecosystems*. Prentice Hall, 592 pp.

Kinar, N. J., and J. W. Pomeroy, 2015: Measurement of the physical properties of the snowpack. *Rev. Geophys.*, **53**, 481–544, https://doi.org/10.1002/2015RG000481.

Kirkham, J. D., and Coauthors, 2019: Near real-time measurement of snow water equivalent in the Nepal Himalayas. *Front. Earth Sci.*, **7**, 177, https://doi.org/10.3389/feart.2019.00177.

Koch, F., M. Prasch, L. Schmid, J. Schweizer, and W. Mauser, 2014: Measuring snow liquid water content with low-cost GPS receivers. *Sensors*, **14**, 20 975–20 999, https://doi.org/10.3390/s141120975.

Lievens, H., and Coauthors, 2019: Snow depth variability in the Northern Hemisphere mountains observed from space. *Nat. Commun.*, **10**, 4629, https://doi.org/10.1038/s41467-019-12566-y.

McCrary, R. R., S. McGinnis, and L. O. Mearns, 2017: Evaluation of snow water equivalent in NARCCAP simulations, including measures of observational uncertainty. *J. Hydrometeor.*, **18**, 2425–2452, https://doi.org/10.1175/JHM-D-16-0264.1.

Ménard, C. B., and Coauthors, 2019: Meteorological and evaluation datasets for snow modelling at 10 reference sites: Description of in situ and bias-corrected reanalysis data. *Earth Syst. Sci. Data*, **11**, 865–880, https://doi.org/10.5194/essd-11-865-2019.

Menne, M. J., and Coauthors, 2012: Global Historical Climatology Network-Daily (GHCN-Daily), version 3.21. NOAA National Climatic Data Center, accessed 27 October 2017, https://doi.org/10.7289/V5D21VHZ.

Meyer, J. D. D., J. Jin, and S.-Y. Wang, 2012: Systematic patterns of the inconsistency between snow water equivalent and accumulated precipitation as reported by the snowpack telemetry network. *J. Hydrometeor.*, **13**, 1970–1976, https://doi.org/10.1175/JHM-D-12-066.1.

Molotch, N. P., and R. C. Bales, 2005: Scaling snow observations from the point to the grid element: Implications for observation network design. *Water Resour. Res.*, **41**, W11421, https://doi.org/10.1029/2005WR004229.

Momblanch, A., I. Holman, and S. Jain, 2019: Current practice and recommendations for modelling global change impacts on water resource in the Himalayas. *Water*, **11**, 1303, https://doi.org/10.3390/w11061303.

Nitu, R., and K. Wong, 2010: CIMO survey on national summaries of methods and instruments for solid precipitation measurement at automatic weather stations. Instruments and Observing Methods Rep. 102, WMO/TD-1544, 57 pp., https://library.wmo.int/doc_num.php?explnum_id=9443.

NSIDC, 2020: All about snow. Accessed August 2020, https://nsidc.org/cryosphere/snow.

Orsolini, Y., and Coauthors, 2019: Evaluation of snow depth and snow cover over the Tibetan Plateau in global reanalyses using in situ and satellite remote sensing observations. *Cryosphere*, **13**, 2221–2239, https://doi.org/10.5194/tc-13-2221-2019.

Pekel, J.-F., A. Cottam, N. Gorelick, and A. S. Belward, 2016: High-resolution mapping of global surface water and its long-term changes. *Nature*, **540**, 418–422, https://doi.org/10.1038/nature20584.

Pounder, E. R., 1965: The mechanical properties of ice. *The Physics of Ice*. Pergamon, 86–115.

Rohrer, M., N. Salzmann, M. Stoffel, and A. V. Kulkarni, 2013: Missing (in-situ) snow cover data hampers climate change and runoff studies in the Greater Himalayas. *Sci. Total Environ.*, **468–469**, S60–S70, https://doi.org/10.1016/j.scitotenv.2013.09.056.

Salzmann, N., C. Huggel, M. Rohrer, and M. Stoffel, 2014: Data and knowledge gaps in glacier, snow and related runoff research – A climate change adaptation perspective. *J. Hydrol.*, **518**, 225–234, https://doi.org/10.1016/j.jhydrol.2014.05.058.

Schattan, P., G. Baroni, S. E. Oswald, J. Schöber, C. Fey, C. Kormann, M. Huttenlau, and S. Achleitner, 2017: Continuous monitoring of snowpack dynamics in alpine terrain by aboveground neutron sensing. *Water Resour. Res.*, **53**, 3615–3634, https://doi.org/10.1002/2016WR020234.

Sideris, I., M. Gabella, M. Sassi, and U. Germann, 2014: The CombiPrecip experience: Development and operation of a real-time radar-raingauge combination scheme in Switzerland. *2014 Int. Weather Radar and Hydrology Symp.*, Washington, DC, American Society of Civil Engineers, 10 pp.

Smith, T., and B. Bookhagen, 2018: Changes in seasonal snow water equivalent distribution in High Mountain Asia (1987 to 2009). *Sci. Adv.*, **4**, e1701550, https://doi.org/10.1126/sciadv.1701550.

Smith, C. D., A. Kontu, R. Laffin, and J. W. Pomeroy, 2017a: An assessment of two automated snow water equivalent instruments during the WMO Solid Precipitation Intercomparison Experiment. *Cryosphere*, **11**, 101–116, https://doi.org/10.5194/tc-11-101-2017.

——, G. van der Kamp, L. Arnold, and R. Schmidt, 2017b: Measuring precipitation with a geolysimeter. *Hydrol. Earth Syst. Sci.*, **21**, 5263–5272, https://doi.org/10.5194/hess-21-5263-2017.

Sommer, W., and R. Fiel, 2009: Snow Pack Analyser (SPA) for snow water equivalent (SWE) and liquid water content. Sommer Messtechnik, accessed August 2020, https://www.sommer.at/en/products/snow-ice/snow-pack-analyzer-spa-2.

Steiner, L., M. Meindl, C. Fierz, and A. Geiger, 2018: An assessment of sub-snow GPS for quantification of snow water equivalent. *Cryosphere*, **12**, 3161–3175, https://doi.org/10.5194/tc-12-3161-2018.

Stigter, E. E., M. Litt, J. F. Steiner, P. N. J. Bonekamp, J. M. Shea, M. F. P. Bierkens, and W. W. Immerzeel, 2018: The importance of snow sublimation on a Himalayan glacier. *Front. Earth Sci.*, **6**, 108, https://doi.org/10.3389/feart.2018.00108.

Stranden, H. B., B. L. Ree, and K. M. Møen, 2015: Recommendations for automatic measurements of snow water equivalent in NVE. Rep. 96-2015, Norwegian Water Resources and Energy Directorate, 34 pp., https://publikasjoner.nve.no/rapport/2015/rapport2015_96.pdf.

Sturm, M., B. Taras, G. E. Liston, C. Derksen, T. Jonas, and J. Lea, 2010: Estimating snow water equivalent using snow depth data and climate classes. *J. Hydrometeor.*, **11**, 1380–1394, https://doi.org/10.1175/2010JHM1202.1.

——, M. A. Goldstein, and C. Parr, 2017: Water and life from snow: A trillion dollar science question. *Water Resour. Res.*, **53**, 3534–3544, https://doi.org/10.1002/2017WR020840.

Tipman, J., 2020: Calibration and use of geolysimeters for the measurement of hydrologic fluxes in mine closure landforms. M.Sc. thesis, University of Saskatchewan, 142 pp., http://hdl.handle.net/10388/13021.

UNESCO/IASH/WMO, 1970: Seasonal snow cover: A contribution to the International Hydrological Decade. Technical Papers in Hydrology Series, United Nations Educational, Scientific and Cultural Organisation, 38 pp.

van der Kamp, G., and H. Maathuis, 1991: Annual fluctuations of groundwater levels as a result of loading by surface moisture. *J. Hydrol.*, **127**, 137–152, https://doi.org/10.1016/0022-1694(91)90112-U.

——, D. Keir, and M. S. Evans, 2008: Long-term water level changes in closed-basin lakes of the Canadian Prairies. *Can. Water Resour. J.*, **33**, 23–38, https://doi.org/10.4296/cwrj3301023.

WMO, 2018: *Measurement of Meteorological Variables. Vol. 1, Guide to Instruments and Methods of Observation*, WMO-8, World Meteorological Organization, 573 pp., https://library.wmo.int/index.php?lvl=notice_display&id=12407#.YCu-03nLdaR.

Wortmann, M., T. Bolch, C. Menz, J. Tong, and V. Krysanova, 2018: Comparison and correction of high-mountain precipitation data based on glacio-hydrological modeling in the Tarim River headwaters (high Asia). *J. Hydrometeor.*, **19**, 777–809, https://doi.org/10.1175/JHM-D-17-0106.1.

Xu, Y., A. Jones, and A. Rhoades, 2019: A quantitative method to decompose SWE differences between regional climate models and reanalysis datasets. *Sci. Rep.*, **9**, 16 520, https://doi.org/10.1038/s41598-019-52880-5.

Yang, D., 2014: Double Fence Intercomparison Reference (DFIR) vs. Bush gauge for "true" snowfall measurement. *J. Hydrol.*, **509**, 94–100, https://doi.org/10.1016/j.jhydrol.2013.08.052.

Yao, H., T. Field, C. McConnell, A. Beaton, and A. L. James, 2018: Comparison of five snow water equivalent estimation methods across categories. *Hydrol. Processes*, **32**, 1894–1908, https://doi.org/10.1002/hyp.13129.

Yatagai, A., K. Kamiguchi, O. Arakawa, A. Hamada, N. Yasutomi, and A. Kitoh, 2012: APHRODITE: Constructing a long-term daily gridded precipitation dataset for Asia based on a dense network of rain gauges. *Bull. Amer. Meteor. Soc.*, **93**, 1401–1415, https://doi.org/10.1175/BAMS-D-11-00122.1.

Yoon, Y., and Coauthors, 2019: Evaluating the uncertainty of terrestrial water budget components over high mountain Asia. *Front. Earth Sci.*, **7**, 120, https://doi.org/10.3389/feart.2019.00120.